Electronic Structure of Niobium and Tantalum

L. F. MATTHEISS
Bell Telephone Laboratories, Murray Hill, New Jersey 07974
(Received 26 June 1969)

The band structures and Fermi surfaces of niobium and tantalum have been calculated via the augmented-plane-wave (APW) method. Relativistic effects have been included in the tantalum but not the niobium calculation. The resulting niobium and tantalum Fermi surfaces are similar to a Fermi-surface model for the vanadium-group transition metals that was proposed previously by the author. This model contains closed hole pockets centered at the symmetry points Γ and N of the bcc Brillouin zone plus a multiply connected hole sheet which extends from Γ to H along ⟨100⟩ directions. Areas and cyclotron masses of closed extremal orbits on the niobium and tantalum Fermi surfaces have been calculated as a function of magnetic field direction in the {100} and {110} planes. The calculated areas are in quantitative agreement with recent experimental results. The maximum discrepancies are 18 and 10% for niobium and tantalum, respectively. The effect of niobium Fermi-surface anisotropy on the temperature dependence of the upper critical field has been evaluated in terms of the Hohenberg-Werthamer theory. The results of this calculation overestimate the experimentally observed effect by a factor of about 2.5.

I. INTRODUCTION

RECENT experiments provide detailed information about the Fermi surfaces of the Group-VB transition metals niobium and tantalum. These include galvanomagnetic,[1,2] magnetothermal oscillation (MTO),[3] and de Haas–van Alphen (dHvA) effect[3–5] studies on single-crystal samples of these materials. The majority of these experimental results have been interpreted in terms of a Fermi-surface model for the vanadium-group transition metals that was derived by the author from a nonrelativistic energy-band calculation for tungsten.[6]

The general features of this vanadium-group Fermi-surface model are illustrated in Fig. 1. The Group-VB transition metals Nb and Ta each contain five conduction electrons per atom, which is one less than W. All three metals crystallize in the bcc structure. In terms of the W band structure, these five electrons fill all of the first, most of the second, and slightly more than half of the third conduction bands. The Fermi-surface sheet which encloses the unoccupied portion of the second zone is shown to the left in Fig. 1. This sheet, which is centered at Γ, has the shape of a rather distorted octahedron. The Fermi-surface sheets which enclose the unoccupied regions of the third zone are shown to the right. These include distorted ellipsoids centered at N and a multiply connected sheet which extends from Γ to H in the ⟨100⟩ directions. This open sheet is referred to as the "jungle gym." In an extended zone scheme, the topology of the jungle gym is equivalent to a ball and stick model for the NaCl structure in which the nearest-neighbor Na^+ and Cl^- ions (different sized balls) are joined by noncylindrical sticks.

The high-field galvanomagnetic data of Fawcett *et al.*[1] confirm that Nb and Ta each possess a holelike Fermi-surface sheet which is equivalent topologically to the jungle gym shown in Fig. 1. The more recent galvanomagnetic measurements of Reed and Soden[2] on higher-purity Nb samples have removed some of the uncertain aspects of the earlier Nb data.[1] These measurements show that the minimum arm diameter of the Nb jungle gym is about 25% smaller than that of Ta. Additional details concerning the Nb and Ta Fermi surfaces are provided by the MTO and dHvA effect data of Halloran *et al.*[3] These data include oscillations which result from extremal orbits on the distorted ellipsoids at N as well as the jungle gym of Fig. 1. In general, these data indicate that the dimensions of the corresponding ellipsoids in Ta are approximately 15% smaller than those in Nb. These data also reflect differences in the jungle-gym dimensions.

The purpose of the present investigation is to provide more detailed theoretical models for the Fermi surfaces of Nb and Ta. These Fermi-surface models have been determined by augmented-plane-wave (APW) calculations involving *ad hoc* "muffin-tin" potentials derived from superposed atomic charge densities.[6] By considering both metals, we hope to understand

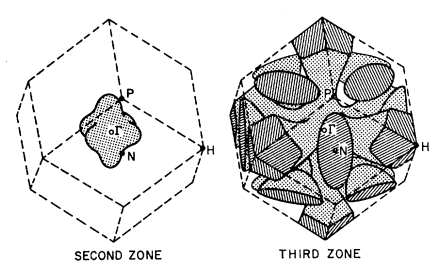

FIG. 1. Fermi-surface model for the vanadium-group transition metals indicating the unoccupied portions of the second and third Brillouin zones.

[1] E. Fawcett, W. A. Reed, and R. R. Soden, Phys. Rev. **159**, 533 (1967).
[2] W. A. Reed and R. R. Soden, Phys. Rev. **173**, 677 (1968).
[3] M. H. Halloran, J. H. Condon, J. E. Graebner, J. E. Kunzler, and F. S. L. Hsu, preceding paper, Phys. Rev. B **1**, 366 (1970).
[4] A. C. Thorson and T. G. Berlincourt, Phys. Rev. Letters **7**, 244 (1961).
[5] G. B. Scott, M. Springford, and J. R. Stockton, Phys. Letters **27A**, 655 (1968).
[6] L. F. Mattheiss, Phys. Rev. **139**, A1893 (1965).

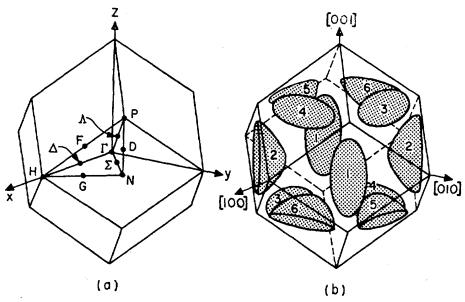

FIG. 2. (a) Brillouin zone for the bcc structure. (b) Arbitrary numbering scheme for distinguishing between the six equivalent distorted ellipsoids at N.

not only the similarities but also the differences in the band structures and Fermi surfaces of these materials.

The calculations have been carried out in two stages. First, the general features of the $5s$-$4d$ conduction bands of Nb and the $6s$-$5d$ conduction bands of Ta were determined using the nonrelativistic APW method. The Darwin and mass-velocity corrections were included in the Ta calculation, using techniques which have been described previously.[7] These energy-band results were used to determine an approximate Fermi energy and Fermi surface for each metal. Then in the final stage of the calculation, surfaces of constant energy were determined directly by fixing the energy E and varying the reduced wave vector $\mathbf{k}$ in the APW method.[8] All relativistic effects including spin-orbit coupling were included in these calculations for Ta. Wave-vector radii $\mathbf{k}(\theta,\Phi;E)$ with origins at Γ, H, and N were used in conjunction with the Mueller inversion scheme[9] to determine central extremal areas and cyclotron masses for closed orbits on the Nb and Ta Fermi surfaces.

The various details of the calculation are summarized in Sec. II. Sec. III contains the energy-band and Fermi-surface results for Nb and Ta. The present APW results for Nb are compared with those calculated by Deegan and Twose[10] using a modified OPW method in Sec. IV. The experimental data relating to the Nb and Ta Fermi surfaces are discussed in Sec. V. Section VI considers the effects of Fermi-surface anisotropy on the temperature dependence of the upper critical field of Nb.

II. DETAILS OF CALCULATION

The present APW calculations involve muffin-tin potentials derived from superposed atomic charge densities.[6] The familiar Slater free-electron exchange approximation[11] has been employed. The Herman-Skillman self-consistent Hartree-Fock-Slater charge density for the atomic configuration $(4d)^4(5s)^1$ was used in the Nb calculation.[12] The corresponding charge density for Ta was provided by Waber; this charge density was obtained from self-consistent Dirac-Hartree-Fock-Slater calculations[13] involving a $(5d)^3(6s)^2$ atomic configuration for Ta. The lattice parameters for Nb and Ta at liquid-helium temperatures were estimated from the room-temperature values and the linear expansion coefficients tabulated by Pearson.[14] The values used in the present calculations are listed in Table I, along with other structure-related information.

The energy bands of Nb and Ta were determined at a total of 1024 uniformly distributed points in the bcc Brillouin zone, which is shown in Fig. 2(a). Here, the standard notation is used to label symmetry points and lines.[15] These energy-band results have been used in conjunction with a crude interpolation scheme to calculate an approximate density of states and Fermi energy.[6] The APW calculations for Nb have been carried out in the nonrelativistic limit. However, the Darwin and mass-velocity corrections have been included in the Ta calculation by replacing the logarithmic derivatives of the radial wave functions at the APW sphere radii

$$(2l+1)u_l'(R,E)/u_l(R,E)$$

by their relativistic equivalent

$$l\eta_l^-(R,E)+(l+1)\eta_l^+(R,E)\,,$$

following the notation of Ref. 7.

Surfaces of constant energy were mapped out in the vicinity of the Fermi energy. These calculations were carried out for three separate energies, E_F and $E_F\pm\Delta$, where E_F is the approximate Fermi energy determined previously and $\Delta=0.005$ Ry. Again, the Nb Fermi-surface calculation was carried out in the nonrelativistic limit. However, all relativistic effects including spin-orbit coupling were included in the Ta calculation. In these calculations, Fermi radii $\mathbf{k}(\theta_i,\Phi_i)$ with an origin at Γ, H, and N were determined by finding roots of the APW secular equation in specific directions (θ_i,Φ_i).[8] Approximately 40 (80) APW functions were included in the nonrelativistic (relativistic) calculations. These included reciprocal-lattice vectors $\mathbf{K}_n$ that approximately satisfied the condition $(\mathbf{k}+\mathbf{K}_n)^2\leq 6.75$ Ry. The lowest seven terms have been included in the spherical harmonic expansion which is contained in the APW matrix elements.[7] These restrictions yield results which converge to within about 0.001 Ry.

The inversion scheme proposed by Mueller[9] has been applied in calculating extremal areas and cyclotron masses for central orbits on the Nb and Ta Fermi

[7] L. F. Mattheiss, Phys. Rev. **151**, 450 (1966).
[8] T. L. Loucks, Phys. Rev. **139**, A1181 (1965).
[9] F. M. Mueller, Phys. Rev. **148**, 636 (1966).
[10] R. A. Deegan and W. D. Twose, Phys. Rev. **164**, 993 (1967).
[11] J. C. Slater, Phys. Rev. **81**, 385 (1951).
[12] F. Herman and S. Skillmann, *Atomic Structure Calculations* (Prentice-Hall, Inc., Englewood Cliffs, N. J., 1963).
[13] D. Liberman, J. T. Waber, and D. T. Cromer, Phys. Rev. **137**, A27 (1965).
[14] W. B. Pearson, *A Handbook of Lattice Spacings and Structure of Metals and Alloys* (Pergamon Press, Inc., New York, 1958).
[15] L. P. Bouckaert, R. Smoluchowski, and E. Wigner, Phys. Rev. **50**, 58 (1936).

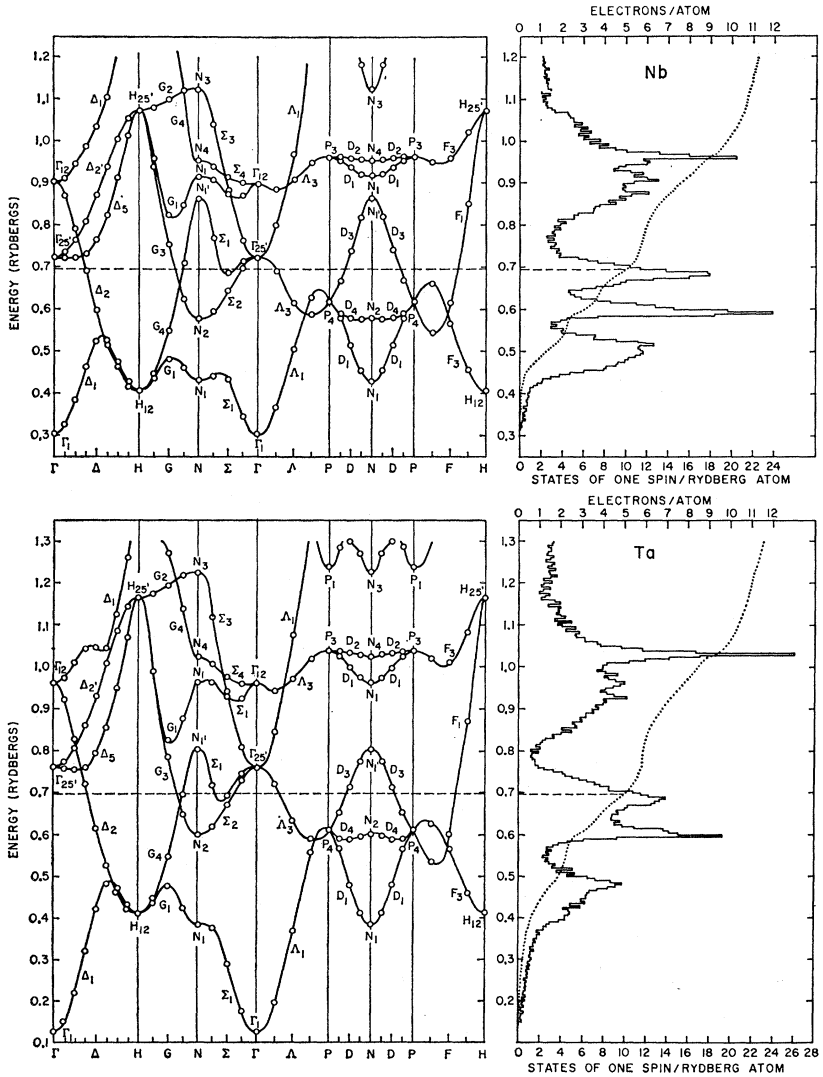

FIG. 3. Energy-band and density-of-states curves for Nb and Ta.

surfaces. This scheme can be applied to closed Fermi-surface sheets which possess a center of inversion and a unique radius vector from this center of inversion. In this method, the square of the wave vector radii $k^2(\theta,\Phi)$ are expanded in lattice harmonics $K_l^i(\theta,\Phi)$ of the appropriate symmetry

$$k^2(\theta,\Phi)=\sum_{l,i}\gamma_l^i K_l^i(\theta,\Phi). \qquad (1)$$

The expansion coefficients γ_l^i are determined by least-squares-fitting procedures. Mueller has shown that the central Fermi-surface area in the plane perpendicular to the (θ,Φ) direction is given by

$$A(\theta,\Phi)=\pi\sum_{l,i}P_l(0)\gamma_l^i K_l^i(\theta,\Phi), \qquad (2)$$

where $P_l(x)$ are Legendre polynomials. The superscript i in Eqs. (1) and (2) labels the linearly independent lattice harmonics which can occur for given value of l.

For Fermi-surface sheets centered at Γ or H in the bcc Brillouin zone, the point-group symmetry is O_h, and the appropriate lattice harmonics are the cubic harmonics, for which extensive tables exist in the literature.[16,17] The corresponding point group symmetry of a Fermi-surface sheet centered at N is D_{2h}', for which lattice harmonics are also available.[17] We have also

TABLE I. Values for the lattice parameters a and the APW sphere radii R used in the present APW calculations for Nb and Ta.

	Nb	Ta
a (a.u.)	6.2294	6.2383
R (a.u.)	2.6974	2.7013

[16] F. M. Mueller and M. G. Priestley, Phys. Rev. **148**, 638 (1966).
[17] S. L. Altmann and A. P. Cracknell, Rev. Mod. Phys. **37**, 19 (1965).

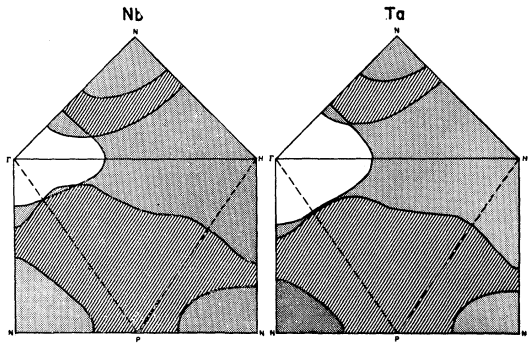

FIG. 4. Central {100} and {110} cross-sections of the Nb and Ta Fermi surfaces.

applied this inversion scheme to the jungle-gym sheet of Fig. 1. This has been done by artificially subdividing this open sheet into two closed sheets, one centered about Γ and the other about H. If the cutoff points on the jungle-gym arms are chosen properly, the resulting surfaces each possess unique radius vectors from Γ and H. The Fermi radii included in the least-squares-fitting procedure are chosen to avoid the neck regions entirely. The inversion scheme closes these surfaces by adding fictitious "tips" on the necks.[18] The resulting areas $A(\theta,\Phi)$ are expected to be accurate except when the orbit passes near these fictitious regions.

In applying this scheme, we have determined the coefficients γ_l^i in Eq. (1) for five separate sets of wave vectors $\mathbf{k}(\theta,\Phi;E)$ corresponding to energies E_F, $E_F\pm\frac{1}{2}\Delta$, $E_F\pm\Delta$. The wave vectors $\mathbf{k}(\theta,\Phi;E_F)$ and $\mathbf{k}(\theta,\Phi;E_F\pm\Delta)$ were calculated directly by the APW method. The intermediate values $\mathbf{k}(\theta,\Phi;E_F\pm\frac{1}{2}\Delta)$ were obtained by interpolation. After calculating $A(\theta,\Phi;E)$ as a function of energy E, the cyclotron mass

$$m_c/m=\frac{\hbar^2}{2m}\frac{\partial A}{\partial E}\bigg|_{E=E_F} \tag{3}$$

has been evaluated by numerical differentiation.

Similar methods have been applied to determine more accurate values for the Fermi energy E_F and the density of states at the Fermi surface $\langle N\rangle$. If $k^3(\theta,\Phi)$ is expanded in lattice harmonics,

$$k^3(\theta,\Phi)=\sum_{l,i}\beta_l^iK_l^i(\theta,\Phi), \tag{4}$$

then the average value of $k^3(\theta,\Phi)$ is $\beta_0^1/(4\pi)^{1/2}$ and the volume enclosed by the surface is $(4\pi)^{1/2}\beta_0^1/3$. Using these methods, we have determined the Fermi energy to within 0.001 Ry by finding the energy at which the total enclosed volume equalled one-half the Brillouin zone volume, or one hole per atom.

The total number of terms which must be included in the expansions of Eqs. (1) and (2) depends on the anisotropy of the surface. By trial and error, we have found that 10 to 15 terms are sufficient in the present calculations to yield 1–2% accuracy in the areas. The coefficients in Eq. (1) were determined by fitting two or three times as many wave-vector radii. The corresponding accuracy of the cyclotron mass results is estimated to be about 5%.

[18] E. I. Zornberg and F. M. Mueller, Phys. Rev. **151**, 557 (1966).

III. RESULTS

The energy-band results for Nb and Ta are shown in Fig. 3, where $E(\mathbf{k})$ curves are plotted along symmetry directions of the bcc Brillouin zone. The corresponding density-of-states curves are shown in histogram form to the right. The dotted line corresponds to the integrated density of states. The Fermi energy is indicated by the dashed horizontal line for each calculation. The energy scale is relative to the constant portion of the muffin-tin potential outside the APW spheres.

The general features of the Nb and Ta energy bands are quite similar to those calculated previously for W.[6] The d bandwidths $[E(H_{25'})-E(H_{12})]$ are approximately 0.7 and 0.8 Ry for Nb and Ta, respectively. In the Ta calculation, the principal effect of the Darwin and mass-velocity corrections is to shift the $6s$, $6p$, and $5d$ states to lower energies by about −0.2, −0.15, and −0.05 Ry, respectively. These effects lower the $6s$, $6p$ bands with respect to the $5d$ states. In particular, the energy difference between the $6p$ state with $N_{1'}$ symmetry and the Fermi energy is decreased in Ta by these relativistic effects.

Central cross sections of the Nb and Ta Fermi surfaces are shown in Fig. 4. The triangular sections ΓHN correspond to central {100} cross-sections while the rectangular portions $\Gamma HNPN$ are central {110} planes. The unshaded regions at Γ represent second zone holes, hereafter abbreviated by OCT. These are contained within the lightly shaded jungle-gym surface (JG). This same shading is used for the distorted

TABLE II. Summary of calculated areas and cyclotron masses for orbits on the Nb and Ta Fermi surfaces.

		Nb		Ta	
H	Sheet	Area (Å^{-2})	m_c/m	Area (Å^{-2})	m_c/m
[001]	JG(Δ)	0.117	−0.57	0.292	−0.84
	ELL(1,2)	0.642	−0.83	0.395	−0.60
	ELL(3,4,5,6)	0.855	−0.97	0.567	−0.78
	JG(M)	1.494	1.74	1.147	1.31
	OCT	0.881	−1.92	1.324	−1.66
[111]	ELL(1,3,4)	0.663	−0.73	0.448	−0.60
	ELL(2,5,6)	0.867	−1.12	0.520	−0.81
	OCT	0.453	−1.54	0.900	−1.68
	JG(Γ)	0.742	−2.29	1.133	−1.94
	JG(H)	1.881	−1.17	1.988	−1.43
[110]	ELL(3,4,5,6)	0.677	−0.70	0.442	−0.61
	ELL(1)	0.762	−0.79	0.562	−0.75
	ELL(2)	0.940	−0.98	0.580	−0.80
	OCT	0.675	−1.66	1.065	−1.46

ellipsoids at N (ELL) since both sheets enclose holes in the third zone.

In the case of Nb, the OCT and JG sheets contact at three points in the {110} and {100} symmetry planes. Along ΓP, this degeneracy is symmetry-induced and is caused by the doubly degenerate Λ_3 state. The other two points of contact are caused by accidental degeneracies between states of even and odd reflection symmetry in these symmetry planes. In the case of Ta, spin-orbit coupling removes these degeneracies between the OCT and JG sheets. However, the magnitude of the spin-orbit induced gaps in quite small. Along ΓP, the spin-orbit splitting is reduced by an accidental crossing of the $\Lambda_{4,5}$ and Λ_6 states that occurs approximately 0.02 Ry below the Ta Fermi energy.

In Fig. 5, we plot the extremal areas and cyclotron masses for central orbits on the various sheets of the Nb and Ta Fermi surfaces as a function of magnetic field direction in the (001) and (1$\bar{1}$0) symmetry planes. The ELL results are shown to the left [Figs. 5(a) and 5(d)], where the various branches are labeled in accordance with the numbering scheme of Fig. 2(b). The corresponding results for the OCT sheet of the Fermi surface are shown by the solid lines in the center portion of Figs. 5(b) and 5(e). The dashed lines correspond to orbits on the JG centered about Γ which are closed when the magnetic field is near [111]. The corresponding results for similar orbits on the JG centered at H are shown to the right [Figs 5(c) and 5(f)]. In general, the cyclotron mass curves exhibit angular variations which scale approximately with the $A(\theta,\Phi)$ curves. In some instances, additional structure is present, particularly in Figs. 5(b) and 5(c). This structure occurs when the velocity vector is nearly perpendicular to the plane of the orbit, at least over a limited region of the Fermi surface.

The calculated areas and cyclotron masses for closed orbits on the Nb and Ta Fermi surfaces with the magnetic field along the three symmetry axes are summarized in Table II. Many of these results are shown in Fig. 5. Two exceptions are the orbits labeled JG(Δ) and JG(M). Both these orbits involve the jungle-gym sheet JG. The first, JG(Δ), is a holelike orbit about one of the JG arms. The other, JG(M), is an electronlike orbit centered at M.

The volumes enclosed by the various Fermi-surface sections have been calculated using the techniques

TABLE III. Contribution of individual Nb and Ta Fermi-surface sheets to the hole density $n(E_f)$ (holes/atom) and density of states $\langle N\rangle \equiv -\partial n(E)/\partial E|_{E=E_f}$ (states of one spin/Ry atom).

	Nb		Ta	
Sheet	$n(E_f)$	$\langle N\rangle$	$n(E_f)$	$\langle N\rangle$
OCT	0.056	1.37	0.128	1.56
ELL	0.429	4.10	0.231	2.71
JG	0.515	4.42	0.641	4.55
Total	1.000	9.89	1.000	8.82

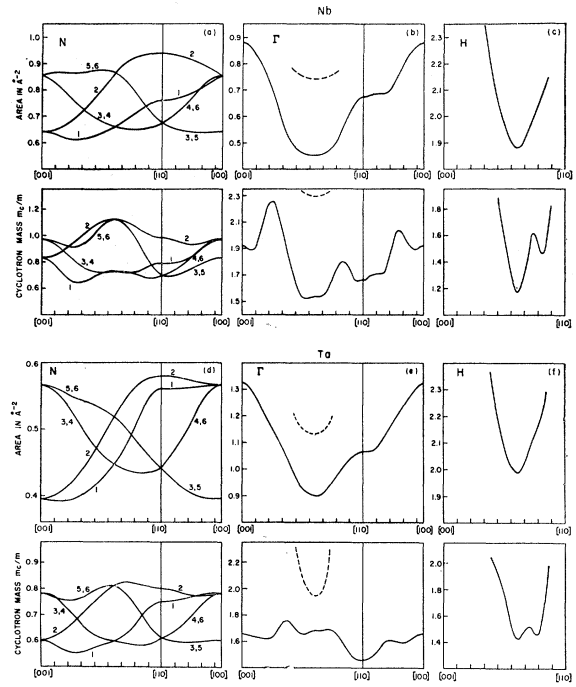

FIG. 5. Extremal areas and cyclotron masses for orbits on various sheets of the Nb and Ta Fermi surfaces.

discussed in connection with Eq. (4). The results are summarized in Table III. These results correspond to a Fermi energy of 0.696 Ry for Nb and 0.697 Ry for Ta. The corresponding values for the density of states $\langle N\rangle$ are approximately 20% smaller than the less accurate values plotted in Fig. 3.

IV. COMPARISON WITH MODIFIED OPW RESULTS FOR Nb

Deegan and Twose[10] have formulated a modified version of the orthogonalized-plane-wave (MOPW) method for calculating the energy bands of transition metals. As an application of this MOPW method, Deegan and Twose have calculated the Nb band structure using a muffin-tin potential which is nearly identical with the one involved in the present APW calculation. The two potentials differ only in the value for the constant potential outside the APW spheres. In the the MOPW calculation, this constant was chosen to make the potential continuous at the sphere radii; in the present APW calculation, the muffin-tin potential contained a discontinuity of 0.034 Ry at the sphere radius. Otherwise, the potentials were identical to within a few thousandths of a rydberg.

After modifying the present Nb muffin-tin potential to remove the discontinuity at R, the energy-band states at symmetry points in the Brillouin zone were calculated using the APW method. These results are compared with the MOPW results of Deegan and Twose in Table IV. The over-all agreement in the results of

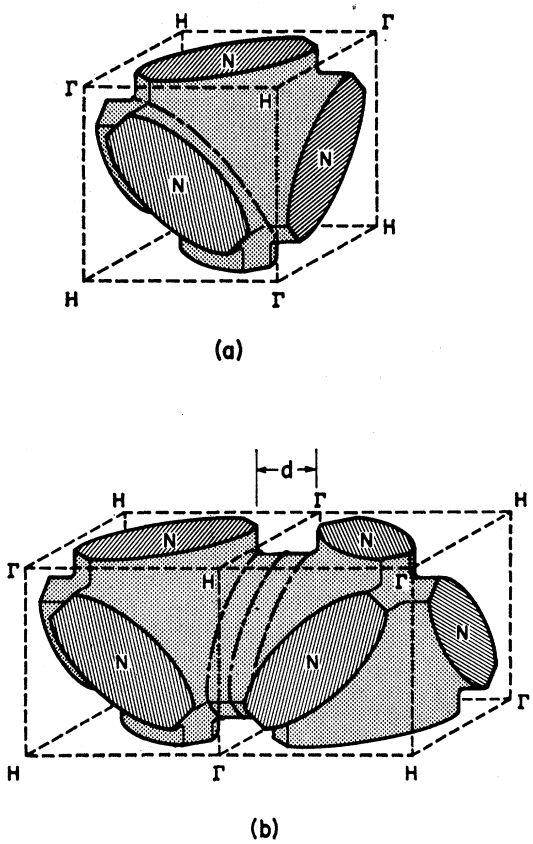

FIG. 6. Sketch of the multiply connected Fermi-surface sheet which encloses occupied portions of the third zone in Nb and Ta.

these two independent calculations for Nb is excellent. The largest difference is 0.01 Ry, which occurs for the $5p$ state with $N_{1'}$ symmetry. The average difference is about 0.003 Ry. This excellent agreement in the energy-band results for Nb by two independent methods represents a convincing test of the numerical procedures involved in each of the calculations.

TABLE IV. Comparison between the modified orthogonalized-plane-wave (MOPW) and APW results for Nb (in rydbergs).

	MOPW[a]	APW
Γ_1	0.318	0.322
Γ_{12}	0.932	0.931
$\Gamma_{25'}$	0.758	0.755
H_{12}	0.434	0.432
$H_{25'}$	1.106	1.108
H_{15}	1.406	1.415
N_1	0.460	0.457
N_1	0.956	0.949
N_2	0.612	0.609
N_3	1.159	1.160
N_4	0.990	0.988
$N_{1'}$	0.873	0.883
P_3	0.998	0.997
P_4	0.645	0.642
P_4	1.563	1.562

[a] Reference 10.

V. DISCUSSION

Our representation of the JG in Fig. 1 as a hole-type surface is somewhat arbitrary. An equivalent representation of this Fermi-surface sheet in terms of an electron-type surface is possible. In this alternative representation, shown in Fig. 6, the surface is drawn to enclose the occupied rather than the unoccupied portions of the third Brillouin zone. The section shown in Fig. 6(a) is centered about P and therefore has tetrahedral point symmetry T_d.[15] For simplicity, we have omitted from this figure the ELL sheets at N. The volume enclosed by the dashed cube in Fig. 6(a) corresponds to one-half that of the bcc Brillouin zone. The broken line in Fig. 6(a) indicates a closed electron orbit that exists when the magnetic field H is near a $\langle 111\rangle$ axis.

A larger section of this sheet is shown in Fig. 6(b). Here, the broken lines are used to indicate electron orbits that are closed when **H** is near a $\langle 001\rangle$ axis. With **H** along [010], these closed orbits exist over a range of k_y values, as indicated by the dimension d in Fig. 6(b). An analogous situation exists in Fig. 6(a) when **H** is along [111]. The dimension d in Fig. 6(b) is determined by the minimum arm diameter of the JG in Figs. 1 and 4.

The Hall data of Refs. 1 and 2 is quite easily understood in terms of Fig. 6. Fawcett, Reed, and Soden observe a decrease in the hole carrier concentration when **H** is along either $\langle 100\rangle$ or $\langle 111\rangle$. From the change in the hole carrier concentration that occurs when **H** is along $\langle 100\rangle$ these authors have determined values for d in Nb and Ta. They obtain the values $d(\text{Nb})=0.21\ \Gamma H$ and $d(\text{Ta})=0.29\ \Gamma H$. These dimensions compare favorably with the calculated d values of $0.185\ \Gamma H$ and $0.285\ \Gamma H$ for Nb and Ta, respectively. A similar dimension can be determined from the Hall data for **H** along $\langle 111\rangle$, but this dimension is not easily related to the details of the Fermi surface.

The present Fermi-surface models for Nb and Ta are consistent with the other details of the galvanomagnetic data and its interpretation,[1,2] including: (1) the state of compensation; (2) the sign of the charge carriers; and (3) the existence of $\langle 100\rangle$ and $\langle 110\rangle$ directed periodic open orbits. The reader is referred to the original papers for a more thorough discussion of these points.

Reference 3 contains a detailed comparison between the present Fermi-surface models for Nb and Ta and the dHvA and MTO data. For the present discussion, we summarize this comparison with the results contained in Table V. For niobium, the experimental Fermi surface areas that are observed when **H** is along the [100], [111], and [110] symmetry directions agree with the calculated results to within 5%. The one ex-

TABLE V. Comparison between calculated and experimental[a] Fermi-surface areas (in Å^{-2}) and cyclotron masses (m_c/m) for Nb and Ta.

	H	Surface	Area (MTO)	Area (APW)	Ratio	Mass (MTO)	Mass (APW)	Ratio
Nb:	[100]	JG(Δ)	0.138	0.117	1.18	1.12	0.57	1.97
		ELL(1,2)	0.630	0.642	0.98	···	0.83	···
		ELL(3,4,5,6)	0.815	0.855	0.95	1.60	0.97	1.65
	[111]	ELL(1,3,4)	0.647	0.663	0.97	1.28	0.73	1.75
		JG(H)	1.862	1.881	0.99	···	1.17	···
	[110]	ELL(3,4,5,6)	0.657	0.677	0.98	1.22	0.70	1.74
		ELL(1)	0.760	0.762	1.00	···	0.79	···
Ta:	[100]	JG(Δ)	0.279	0.292	0.96	1.35	0.84	1.61
		ELL(1,2)	0.436	0.395	1.10	1.09	0.60	1.82
	[111]	ELL(1,3,4)	0.472	0.448	1.05	1.06	0.60	1.77
		ELL(2,5,6)	0.550	0.520	1.06	···	0.81	···
		JG(H)	1.976	1.988	0.99	···	1.43	···
	[110]	ELL(3,4,5,6)	0.472	0.442	1.07	1.18	0.61	1.94
		ELL(1)	0.530	0.562	1.03	1.35	0.75	1.80

[a] Reference 3.

ception is the minimum area on the jungle-gym arm JG(Δ) which is 18% smaller than the experimental value. Similar comparisons for Ta produce over-all agreement in the extremal areas to within 10%.

The corresponding mass ratios are much larger. These range from 1.65 to 1.97 in Nb and 1.61 to 1.94 in Ta. It is now well known that the experimental values for the cyclotron mass are enhanced by electron-phonon interactions. McMillan[19] has calculated an average over the Fermi surface of the enhancement factor $(1+\lambda)$ for Nb and Ta. These enhancement factors are 1.82 and 1.65 for Nb and Ta, respectively. The results of Table V are in reasonable agreement with McMillan's values. Neither the theoretical Fermi-surface model nor the experimental data is sufficiently accurate to attribute any real significance to the range of values that are obtained by these ratios.

McMillan has also determined the band density of states at the Fermi surface for Nb and Ta from the superconducting transition temperature, Debye Θ, and specific heat γ. He obtains values of 12.4 and 10.5 states of one spin/Ry atom for Nb and Ta, respectively. Ironically, the less accurate density-of-states results of Fig. 3 are in better agreement with the experimental data.

VI. EFFECT OF Nb FERMI-SURFACE ANISOTROPY ON $H_{c2}(T/T_c)$

Niobium is a type-II superconductor with a zero-field transition temperature $T_c=9.23$°K. Experimental values for the temperature dependence of the upper critical field $H_{c2}(T/T_c)$ of Nb[20] systematically lie above the theoretical curve predicted by Helfand and Werthamer,[21] which is based on a spherical Fermi-surface model for Nb. In the Helfand-Werthamer theory, the upper critical field is normalized and expressed in terms of the dimensionless quantity

$$h(t)\equiv H_{c2}(t)/(-dH_{c2}(t)/dt)_{t=1}, \tag{5}$$

where t is the reduced temperature T/T_c. The Helfand-Werthamer theory has been extended by Hohenberg and Werthamer[22] to include effects due to Fermi-surface anisotropy on $H_{c2}(T/T_c)$. Hohenberg and Werthamer show that Fermi-surface anisotropy can enhance the results of the spherical model by a factor $\exp\alpha$, where α is positive and is defined in terms of an integral over the Fermi surface,

$$\alpha\equiv-\int d\hat{q}\frac{N(\hat{q})}{\langle N\rangle}\ln\frac{v^2(\hat{q})}{\langle v^2\rangle}. \tag{6}$$

Here, $N(\hat{q})$ and $v^2(\hat{q})$ are the density of states and square of the Fermi velocity in the $\hat{q}$ direction, respectively. The averages of these quantities over all directions are represented by $\langle N\rangle$ and $\langle v^2\rangle$, respectively. Although the above theoretical results were obtained in the weak-coupling limit[19] where $\lambda\ll1$, Werthamer and McMillan[23] have shown that since strong-coupling effects are temperature-independent, they cancel out in Eq. (5) for $h(t)$.

We have evaluated the integral in Eq. (6) using the present Fermi-surface model for Nb. In this calculation, we have replaced the integral over all directions $\hat{q}$ by a sum of three integrals over each of the three Fermi-surface sheets OCT, JG, and ELL. For each sheet, the wave vector radii $\mathbf{k}(\theta,\Phi;E)$ were expressed in terms of lattice harmonic expansions analogous to those in Eq. (1), again using least-squares-fitting procedures to determine the expansion coefficients. These expansions were then used to determine Fermi radii on a grid

[19] W. L. McMillan, Phys. Rev. **167**, 331 (1968).
[20] T. Ohtsuka and N. Takano, J. Phys. Soc. Japan **23**, 983 (1967).
[21] E. Helfand and N. R. Werthamer, Phys. Rev. **147**, 288 (1966).
[22] P. C. Hohenberg and N. R. Werthamer, Phys. Rev. **153**, 493 (1967).
[23] N. R. Werthamer and W. L. McMillan, Phys. Rev. **158**, 415 (1967).

TABLE VI. Theoretical values for the average Nb Fermi velocity (cm/sec) and the contribution of individual Nb Fermi-surface sheets to the integral defined by Eq. (6).

Sheet	$[\langle v^2\rangle_{bs}]^{1/2}$	α
OCT	0.40×10^8	0.151
ELL	0.72×10^8	−0.095
JG	0.57×10^8	0.254
Av	0.62×10^8	0.310

similar to that described in the Appendix of Ref. 24. In this scheme, the volume enclosed by each Fermi-surface sheet is subdivided into tetrahedra with edges formed by radii in three neighboring directions. The contribution of the ith tetrahedron to the density of states is proportional to $\Delta V_i/\Delta E$, where ΔV_i is the volume change per energy interval ΔE. If ΔS_i is the element of Fermi-surface area intersected by the three neighboring radii, the square of the local Fermi velocity v_i^2 is proportional to $[\Delta E/\Delta k_i]^2$ or $\Delta E^2[\Delta S_i/\Delta V_i]^2$, since the change in wave vector Δk_i per energy interval ΔE is perpendicular to ΔS_i.

In these calculations, care has been taken to avoid the fictitious regions on the arms of the JG, which are described in Sec. II. The values for the Fermi velocity squared, averaged over the individual Fermi-surface sheets as well as the entire Fermi surface, are listed in Table VI. The individual contributions of the various Fermi-surface sheets to the integral in Eq. (6) are also listed in this table. Summing over all sheets, we find that $\alpha=0.31$, so that $\exp\alpha=1.36$. Experimentally, this enhancement factor is only 1.13,[20] so the present calculations tend to overestimate this effect.

The theory of Hohenberg and Werthamer also predicts a relationship between $\langle v^2\rangle$ and the slope of the $H_{c2}(T/T_c)$ curve at $T=T_c$. They show that[22]

$$\langle v^2\rangle=-\frac{6c(2\pi k_BT_c)^2}{7\zeta(3)ehH'_{c2}(1)}=\frac{2.705\times10^{18}}{-H'_{c2}(1)}\left(\frac{\text{cm}}{\text{sec}}\right)^2. \quad (7)$$

This result was derived in the weak-coupling limit. As noted by Werthamer and McMillan,[23] the main effect of the phonons is to renormalize the Fermi velocity by the factor $(1+\lambda)$. In addition to this normal-state effect, the analysis of Eilenberger and Ambegaokar[25] shows that there is an intrinsically superconducting effect expressed by their Eq. (4.13) which enters Eq. (7) as a second factor. This factor has been estimated by McMillan and Hohenberg[26] to be 1.4 for Nb. Thus, for Nb, Eq. (7) becomes

$$\langle v^2\rangle=\frac{2.705\times10^{18}}{-H_{c2}'(1)}(1+\lambda)^2(1.4)\left(\frac{\text{cm}}{\text{sec}}\right)^2. \quad (8)$$

Using the experimental value for $-H_{c2}'(1)$ from Ref. 20, we find $\langle v^2\rangle_{\text{exp}}=0.26\times10^{16}(\text{cm/sec})^2$ or $\langle v\rangle_{\text{exp}}\equiv[\langle v^2\rangle_{\text{exp}}]^{1/2}=0.51\times10^8$ cm/sec. From the results of Table VI, the theoretical band-structure Fermi velocity for niobium $\langle v\rangle_{bs}=0.62\times10^8$ cm/sec. Thus, the calculated Fermi velocity is about 20% larger than the experimental value.

The simplest explanation for the discrepancy between $\langle v\rangle_{\text{exp}}$ and $\langle v\rangle_{bs}$ is to assume that the Nb $4d$ bandwidth is overestimated by 20% in the present calculation. Such a reduction in the $4d$ bandwidth would reduce the the 30% discrepancy between the calculated and measured band density of states that was noted in the previous section. The results of previous band-structure calculations for tungsten[6] indicate that the uncertainties in the *ad hoc* crystal potential are sufficient to explain a 20 or 30% error in the d bandwidth without introducing any major changes in the detailed Fermi-surface shape and size. Such a reduction in the Nb $4d$ bandwidth will not affect the calculated value for α in Table VI since only the ratios $N(\hat{q})/\langle N\rangle$ and $v^2(\hat{q})/\langle v^2\rangle$ enter in Eq. (6).

An alternative explanation of this discrepancy involves an increase in the renormalization factor $(1+\lambda)$. If the coupling constant λ were isotropic over the entire Fermi surface, this would improve the agreement between $\langle v\rangle_{\text{exp}}$ and $\langle v\rangle_{bs}$. Once again, it would not alter the calculated value of α. Both discrepancies could be resolved, however, by assuming that the coupling constant λ varied for different orbits on the Nb Fermi surface.

ACKNOWLEDGMENTS

The author has benefitted from numerous conversations with his colleagues regarding various aspects of this investigation. These include discussions with M. H. Halloran, J. H. Condon, W. A. Reed, W. L. McMillan, and P. C. Hohenberg. The author is also grateful to J. T. Waber for providing the atomic charge density for Ta that has been used in this calculation.

[24] J. S. Faulkner, H. L. Davis, and H. W. Joy, Phys. Rev. **161**, 656 (1967).

[25] G. Eilenberger and V. Ambegaokar, Phys. Rev. **158**, 332 (1967).

[26] W. L. McMillan and P. C. Hohenberg (private communication).

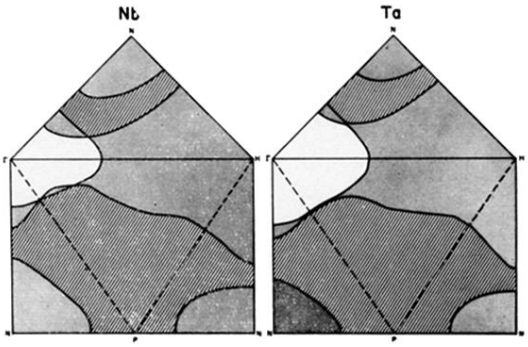

FIG. 4. Central {100} and {110} cross-sections of the Nb and Ta Fermi surfaces.